Infrared Thermal Imagery of Cloud Base in Tornadic Supercells

Robin L. Tanamachi

Howard B. Bluestein

School of Meteorology, University of Oklahoma, Norman, Oklahoma

Stephen S. Moore

Intrinsic Energies Indications, Saline, Michigan

Robert P. Madding

Infrared Training Center, FLIR Systems, Inc., Billerica, Massachusetts

Journal of Atmospheric and Oceanic Technology

Submitted, 5 July 2005

Revised, 3 April 2006

Corresponding author address:

Robin Tanamachi

University of Oklahoma

School of Meteorology

100 E Boyd St.

Norman, OK 73019

rtanamachi@ou.edu

ABSTRACT

During the spring seasons of 2003 and 2004, an infrared thermal camera was deployed in and around supercell thunderstorms in an attempt to retrieve temperature at the cloud base of a mesocyclone prior to tornadogenesis. The motivation for this exercise was to obtain temperature information that might indicate the thermal structure, timing and extent of the rear-flank downdraft (RFD) and possibly elucidate its relationship to tornadogenesis.

An atmospheric transmissivity study was conducted to account for the effects of atmospheric transmission on the measured temperatures, and to determine an ideal range of distances from which infrared images of a wall cloud or a tornado could be safely captured while still retrieving accurate cloud temperatures. This range was found to be 1.5 to 3 km.

Two case days are highlighted in which the infrared camera was deployed within 1.5 to 3 km of a tornado; the visible and infrared images are shown side-by-side for comparison. On the single occasion on which the tornadogenesis phase was captured, the infrared images show no strong horizontal temperature gradients. From the infrared images taken of tornadoes, it can be inferred that the infrared signal from the tornado consisted primarily of infrared emissions from lofted dust particles or cloud droplets, and that the infrared signal from the tornado condensation funnel was easily obscured by infrared emissions from lofted dust particles or intervening precipitation curtains.

The deployment of the infrared camera near supercell thunderstorms and the analysis of the resulting images proved challenging. It is concluded that the infrared camera is a useful tool for measuring cloud base temperature gradients provided that

distance and viewing angle constraints are met and that the cloud base is unobscured by rain or other intervening infrared emission sources. When these restrictions were met, the infrared camera successfully retrieved horizontal temperature gradients along cloud base and vertical temperature gradients (close to the moist adiabatic lapse rate) along the tornado funnel.

1. INTRODUCTION

Cloud base characteristics are determined by the thermodynamic and air flow characteristics of the air in which the clouds form. In a supercell thunderstorm, variations in the height of the cloud base, which can be relatively sharp, can indicate distinct thermodynamic and air flow characteristics of adjacent air masses.

Tornado formation in supercell thunderstorms is frequently observed near the updraft-downdraft interface in a "divided" mesocyclone (Fig. 1; Lemon and Doswell 1979; Doswell 1985). It has been suggested that the temperature field in and near a low-level mesocyclone, particularly that associated with the rear-flank downdraft (RFD), may play a role in tornadogenesis (Davies-Jones *et al.* 2001; Markowski *et al.* 2002). Previous field studies tested this hypothesis using mobile *in situ* instruments to measure thermodynamic variables in and around the tornado's parent mesocyclone. While the collection of mobile *in situ* data was often successful, the usefulness of the data was somewhat limited by the confinement of most of the measuring instruments to the level nearest the surface, which resulted in 1D or quasi-2D measurements. Comprehensive summaries of these study efforts can be found in Markowski (2002a) and Bluestein (1999). It is currently thought that the relationship between the RFD and tornadogenesis remains, at best, "confusing" (Markowski 2002a), the same conclusion reached by Doswell (1985).

RFDs are herein defined as "regions of subsiding air that develop on the rear [with respect to storm motion] side of the main updraft of supercell storms" (Markowski 2002a). An RFD is often visually manifest as a "dry intrusion" or "clear slot" in the base of a supercell (Fig. 2), which results from evaporation of cloud droplets in the air that is

advected downward and which usually has a relatively low wet-bulb potential temperature (θ_w). The appearance of a clear slot has frequently been observed to precede the appearance of a tornado by a few minutes. Upon reaching the surface, the air in the RFD spreads out horizontally. The leading edge of this air is called a "rear-flank gust front," and it is usually marked by a shift in wind direction at the surface. This shift in wind direction depends upon the location of the observer and the life cycle stage of the mesocyclone. An observer located south of the mesocyclone will usually experience a wind shift from southeasterly (easterly) to northerly or northwesterly (southerly) in the vicinity of a mature (occluded) mesocyclone. Observations collected within supercell storms indicate that the air behind the rear-flank gust front may be significantly colder (e.g., Dowell and Bluestein 1997), the same temperature, or even warmer (e.g., Bluestein 1983) than the air ahead of it.

It has been hypothesized that the absence of a temperature (and hence, buoyancy) gradient across the rear-flank gust front may be a necessary but not sufficient condition for the formation of significant tornadoes (Markowski *et al.* 2002). Markowski (2002a) reviewed numerical simulations of supercell thunderstorms, and remarked that these simulations consistently produced "cool" RFDs, even though "warm" or "neutral" RFDs are sometimes observed in nature. It was suggested that the microphysics parameterizations in the numerical models were responsible for this unrealistic characteristic. For this reason, an observational approach to evaluating the temperature gradients along the cloud base in supercell thunderstorms has been favored over numerical simulations.

It is also important to consider the origin of air parcels entering the cloud base near where tornadoes form. In Fig. 1, it is seen that air in the updraft may come from the RFD, from the environment ahead of the storm, or from the forward-flank downdraft (FFD). The height of the cloud base and its temperature can yield information about where the air entering into it originated. For example, Rotunno and Klemp (1985) showed how cooler, more humid air from the FFD entering the updraft base can produce a lowered cloud base, the wall cloud. Variations in temperature and height of the cloud base associated with the updraft may yield clues as to where the air came from.

One of the factors limiting previous observational studies in supercells has been safety; the safe deployment of thermodynamic measuring instruments in a dense network close to a tornadic mesocyclone is extremely difficult. Another limitation has been the relative scarcity of *above-surface* 2D and 3D thermodynamic observations in this region; observational studies conducted during VORTEX and other field experiments have been largely limited to 1D and quasi-2D surface observations (e.g., Markowski *et al.* 2002). The following study was motivated by the desire to address these two limitations.

Infrared thermal imagery, or thermography, can be used to infer the temperature of objects from the images of their emitted long wave infrared radiances. Infrared thermal imagery is familiar to the general public through its industrial, military, and law enforcement applications (Holst 2000; Burnay *et al.* 1988). Infrared thermal imagery has been used extensively in meteorological applications involving satellite infrared thermal imagers (Kidder and Vonder Haar 1995; Burnay *et al.* 1988; Liou 2002) and ground-based, skyward-pointing atmospheric infrared detectors (e.g., Knuteson *et al.* 2004), both

of which are designed primarily for the purpose of deducing the thermal structure of the atmosphere as a function of altitude over a point on the earth's surface.

In this study, a digital infrared camera was used in an attempt to distinguish among different stages in the life cycle of a tornado based on the measured thermal characteristics of the visible tornado and surrounding cloud base. This study marks the first known use (to the best knowledge of the authors) of ground-based digital infrared thermography for severe storms research.

In order to determine what type of temperature gradients we might anticipate measuring along a tornadic supercell cloud base, the temperature and cloud water mixing ratio fields of a numerically simulated tornadic supercell (M. Xue, personal communication) were examined. Qualitatively, the structure of the temperature field at the cloud base of the numerically simulated supercell was roughly representative of the structure of the temperature field at the surface. From the results of these and other simulations (e.g., Rotunno and Klemp 1985), it was inferred that temperature gradients on the order of 5 °C km^{-1} or less could potentially be anticipated along a cloud base in the vicinity of a tornado.

In effect, it was assumed in this study that the cloud base temperature field was qualitatively representative of the temperature field at the surface. The validity of this assumption remains an open question and its evaluation is beyond the scope of this study. To determine the extent cloud-base temperatures would actually be useful in estimating horizontal temperature gradients at the surface and thus to be able estimate the rate of baroclinic generation of horizontal vorticity, 3D, *in situ* measurements would be required

and/or an extensive set of high-resolution numerical experiments would need to be conducted.

The infrared camera was deployed near numerous supercell thunderstorms in 2003 and 2004 (Fig. 3). The infrared camera used was a tripod-mounted, digital, FLIR Systems brand S60 ThermaCam digital radiometric imager (Fig. 4) capable of detecting infrared radiation in wavelengths between 8 and 12 μm at a resolution of 320 × 240 pixels. The 8 – 12 μm band is a water vapor "window," wherein water vapor has relatively low emissivity and absorptivity, and therefore a relatively small effect on atmospheric transmissivity. As will be discussed later, the use of this wavelength band posed difficulties. The infrared camera and its software were designed primarily for the examination of solid objects at close range, while minimizing the effects of emissions from the intervening air. An RFD itself could not be imaged, as it would be composed mostly of clear air. Air temperatures had to be inferred from the temperatures of infrared emitters that were present in the air nearby (cloud droplets, dust, etc.).

The infrared camera was also equipped with a low-resolution (640 × 480 pixels) digital camera, enabling the thermographer to capture a corresponding visible image within a few seconds of the infrared image capture. Side-by-side analysis of the visible and infrared images was therefore possible.

Section 2 details the atmospheric transmissivity issues related to this study. In Section 3, two cases are highlighted in which side-by-side visible and infrared thermal images of tornadoes and their attendant cloud bases are examined. In Section 4, interpretations and conclusions are presented.

2. ATMOSPHERIC TRANSMISSIVITY STUDY

An atmospheric transmissivity study was conducted to determine the effect of atmospheric attenuation on the infrared signal from cloud base. Infrared thermal images were captured of low-level, cumuliform, non-precipitating water clouds above the National Weather Service (NWS) office in Norman, Oklahoma. These images were captured at the same time as standard NWS 00 UTC rawinsonde launches. Cloud-base temperatures measured by the infrared camera were then compared with the lower atmospheric profile measured by the rawinsonde.

Clouds composed of water droplets and of sufficient thickness to be classified as opaque generally behave like blackbodies (Liou 2002); a cloud emissivity of 0.98 (the default setting of the infrared camera) was assumed. The present transmissivity study made use of the assumption that (1) the cloud base height was the same as the lifting condensation level (LCL) height calculated for a parcel representative of the mean measurements collected in the lowest 500 m of the atmosphere by the rawinsonde, and (2) the temperature of the cloud droplets in the cloud base was the same as the corresponding calculated LCL temperature. The errors in the LCL height (±50 m; Craven *et al.* 2002) and LCL temperature (±0.5 K at 800 mb) calculated from the rawinsonde measurements were assumed to be negligible for the purposes of this study. The small amount of heating caused by latent heat release from condensation (Wallace and Hobbs 1977) was also assumed to be negligible since the temperature change due to this heating probably occurred at a slow rate during cloud formation, falling within the range of spectral noise of the infrared camera (± 2 °C).

The approximate line-of-sight distance from the infrared camera to a selected cloud base was computed from the elevation angle of the camera using simple

trigonometry, and the height of the LCL was computed from the rawinsonde observations. The computed line-of-sight distance and known ambient atmospheric conditions were entered into proprietary ThermaCam software designed to correct the measured temperatures in the images for clear-air atmospheric attenuation by water vapor, using a simplified version of the MODTRAN radiative transfer model (Berk *et al.* 1989). The atmospheric attentuation of the intervening air was approximated using the measured relative humidity of the ambient atmosphere and an empirically-fit cubic function of the measured ambient atmospheric temperature.

The limitations of this simplified model became apparent when the "corrected" temperature of the cloud base as measured by the infrared camera was compared with the LCL temperature calculated from the rawinsonde measurements. The three primary causes of erroneous temperature readings in the atmospheric transmissivity study were as follows: (1) infrared-emitting constituents (such as haze and ozone) in the planetary boundary layer contaminated cloud temperature measurements at low elevation angles, causing the measured temperatures of cloud base at these low elevation angles to be too warm. (2) All objects in a given infrared image were assumed by the camera software to be at the same distance from the infrared camera. If the distance setting of the infrared camera was too large, the camera software overcompensated for atmospheric attenuation, and the cloud appeared to be too warm. If the distance setting was too small, the camera software undercompensated for atmospheric attenuation, and the cloud appeared to be too cold. (3) If the cloud was not optically thick, or there were breaks in the clouds, the cold upper troposphere or colder or more distant clouds were "visible" through the cloud in

the infrared, and the cloud appeared to be too cold. These sources of cloud base temperature measurement error are depicted in Fig. 5.

In the present study, the proprietary ThermaCam software correction compensated well for the erroneous camera settings, but not as well for the optically thin clouds or for the infrared emissions from boundary layer gases and particles. An apparent positive correlation between the concentration of infrared emitters (such as haze) in the lowest levels of the troposphere and the air temperature near the surface was observed, implying that the error source described in Fig. 5a would have a greater effect at higher surface air temperatures.

As the camera was tilted towards the horizon, the optical depth of the intervening atmosphere decreased owing to the relatively high concentrations of water vapor, ozone, and other infrared-emitting gases and particulates in the planetary boundary layer. Just above the horizon, the infrared signal from the distant cloud base became entirely obscured by these nearer infrared emission sources (Fig. 6). Thus, the measured temperatures of clouds near the horizon were unrealistically high. In general, low clouds appeared warmer than their surroundings when the camera elevation angle was greater than 30°, owing to their contrast against cooler upper tropospheric air or colder clouds at higher elevations.

The data used in the transmissivity study are plotted in Fig. 7. The difference between the "corrected" temperature of the cloud base as measured by the infrared camera and the rawinsonde became more negative as the distance of the cloud base from the infrared camera increased. At the shortest distances (less than 1.5 km) the temperatures measured by the infrared camera, which were inferred from infrared images

collected while the camera was pointing straight up, were much cooler than those recorded by the rawinsonde. This error probably resulted from contamination of the cloud temperature measurement by the clear sky above, i.e., the clouds were not optically thick enough to completely obscure the infrared signal from the cold upper troposphere. Thunderstorm clouds are optically very thick, and so this potential source of temperature measurement error was not considered in the study of tornadic supercells discussed in the next section.

The shaded box in Fig. 7 encloses a region that represents an optimum distance for temperature measurement between the camera and the cloud base, between approximately 1500 and 3000 m (1.5 and 3.0 km). In this region, the difference between the temperature measured by the rawinsonde and that measured by the infrared camera was most consistently close to zero; thus, it is reasonable to suggest that 1.5 to 3.0 km is the best range from which to study temperature changes accurately (and, in the case of mesocyclones, safely) across low cloud bases. This finding agrees to some extent with that of Holst (1996), who found that atmospheric transmissivity decreases markedly in the 8-12 μm band at ranges between 2 and 5 km.

Even within this "best range" of 1.5 to 3.0 km, errors of up to ±4 °C were still present. Changes in air temperature of even a few degrees can significantly impact thunderstorm dynamics. Therefore, the primary focus of the next section will be on the measured *gradients* of temperature along the cloud base in tornadic thunderstorms, rather than on the temperature measurements themselves.

3. INFRARED THERMAL IMAGERY IN TORNADOES

During the spring seasons of 2003 and 2004, the infrared camera was deployed near supercell thunderstorms (e.g., Fig. 3). The goal of each infrared camera deployment was the capture of infrared images within 3 km of a wall cloud associated with a tornadic mesocyclone. The 3 km distance criterion, derived from the transmissivity study described in the previous section, was intended to ensure that the camera would be close enough to distinguish the infrared signal of the cloud base from that of the intervening atmosphere. There were nine deployments in 2003 and 16 deployments in 2004. The deployments occurred alongside a mobile radar unit (e.g., Kramar *et al.* 2005; Bluestein *et al.* 2004; Wurman and Gill 2000) whenever possible, in order to ascertain an accurate line-of-sight distance between the infrared camera and developing tornadoes. What follows is discussion of the two most successful case days and the infrared images captured on each.

a. 12 May 2004: Harper Co., Kansas

On 12 May 2004 (local time), a storm intercept team from the University of Oklahoma (OU) documented at least seven tornadoes in a supercell thunderstorm that occurred over Harper County, Kansas. The National Weather Service office in Wichita, Kansas documented eleven separate tornadoes in this supercell (Hayes 2004). Over 100 infrared images of tornadoes and their associated cloud base prior to tornadogenesis were captured in three separate infrared camera deployments (Fig. 8). In addition, a mobile, 3-mm wavelength (W-band) Doppler radar (Bluestein *et al.* 2004) and a mobile, 3-cm wavelength (X-band) Doppler radar (Bluestein *et al.* 2005a, Kramar *et al.* 2005) from the University of Massachusetts were deployed. Radar data was collected in several

tornadoes, and the exact distance between the infrared camera and each tornado was thereby ascertained.

1) Deployment #1

The first tornado recorded by the OU storm intercept team formed at approximately 0015 UTC on 13 May, southeast of the town of Sharon, Kansas (Fig. 9a). The tornado was already in the mature stage of its life cycle when first observed by the storm intercept team; therefore, no infrared images during tornadogenesis were captured during this deployment. No distinct RFD-generated clear slot was observed from the location of the infrared camera. The tornado formed at a distance of approximately 5.2 km from the storm intercept team, well outside of the "ideal" range of 1.5 to 3.0 km. From the location of the infrared camera, the condensation funnel of the tornado appeared to be tilted at an angle of approximately 45º with respect to the ground. It is evident from reflectivity data collected in this tornado by the W-band and X-band mobile radars that the tornado apparently moved a distance of less than 1 km towards the east, and dissipated at approximately 0022 UTC. This tornado received a rating of F0 on the Fujita scale (NCDC 2004a).

The infrared images do not show a distinct infrared signal from the tornado funnel itself (Fig. 9b) because the tornado occurred at a long distance from the infrared camera. For this reason, a detailed analysis of the temperature gradients across and along the tornado funnel and its associated cloud base could not be performed. Infrared-emitting constituents of the boundary layer probably heavily contaminated the infrared signal, if any, from the tornado and its associated cloud base (in a manner similar to that described in Section 2).

2) Deployment #2

Another tornado formed at approximately 0055 UTC, approximately 2.8 km southwest of the storm intercept team, and approximately 1.5 km southeast of the town of Attica, Kansas (Fig. 8). A sequence of 29 infrared images was captured during this deployment. During tornadogenesis, no temperature difference greater than that of instrument noise was observed across the base of the mesocyclone lowering in the vicinity of the visible tornadic circulation (Fig. 9d-i). The RFD-generated "clear slot" is visible in Fig. 9d and 9g; a small decrease (on the order of 1 ºC) in the temperature of nearby cloud droplets can be observed near the clear slot prior to and during tornadogenesis (Fig. 9d, e, g, and h). Although the temperature decrease falls within the range of instrument noise (±2 °C), the pattern of measured temperatures along the edges of the infrared "clear slot" appears to be spatially and temporally coherent. Whether this feature is indicative of an actual decrease in temperature resulting from entrainment of RFD air at the downdraft-updraft interface, an apparent decrease resulting from the infrared measurement of temperature of cloud droplets on the far side of the RFD versus those on the near side in the same infrared image, or a mixture of both, is not known.

The tornado developed a large, dusty funnel as it traversed open fields, and received a rating of F2 on the Fujita scale as a result of damage to the roof of a house (NCDC 2004a). Detailed Doppler-radar analyses of this and the remaining tornadoes on this day can be found in Bluestein *et al.* (2005a, b).

During its mature phase, the tornado tracked slightly to the north-northwest, and crossed U.S. Highway 160 near Attica, Kansas at 0102 UTC on 13 May 2004 at a distance of approximately 3.0 km from the storm intercept team (Fig. 8). The tornado

(Fig. 9j) appeared in the infrared imagery (Fig. 9k) as a column of slightly elevated temperatures approximately 600 m in diameter; the shape of this column did not coincide exactly with the visible shape of the conical tornado condensation funnel. The infrared signal of the conical tornado condensation funnel, which was expected to appear as a similarly-shaped area of slightly cooler temperatures resulting from adiabatic cooling of the air induced by the decrease in atmospheric pressure, was either very faint or nonexistent in almost all of the infrared images.

The mobile X-band radar presentation of this tornado (not shown) contains a circular region with a diameter of approximately 900 m of relatively low differential reflectivity (Z_{DR}) at an altitude of approximately 200 m AGL (Bluestein *et al.* 2005a). It is suggested, based on the diameter and spatial coherence of the low-Z_{DR} feature, that this circular region of low Z_{DR} represents the horizontal extent of the dust cloud at the level of the radar scan. The diameter of the column of slightly elevated temperatures was increasingly obscured near the ground, where, as the transmissivity study indicated, infrared signal contamination due to haze and lofted soil particles was probably high. In general, the measured temperatures in the lower portion of the tornado were probably representative of lofted dust particles from the warm surface soil layer in the tornado, and the measured temperatures in the upper portion of the tornado were probably more representative of cloud droplets in the condensation funnel (e.g., Fig. 9j, k). Judging from the visual appearance of the tornado in Fig. 9j, the column of elevated temperatures in Fig. 9k was probably the result of lofted dust from the surface to just below the level of the cloud base.

The vertical temperature gradient retrieved along the temperature trace LI04, along the tornado funnel, was -5.5 ºC km^{-1}. Interestingly, this lapse rate is close to, but not equal to, the moist adiabiatic lapse rate in the lower troposphere at a temperature of 20 ºC, which is -4.3 ºC km^{-1} (Curry and Webster 1999). It is suggested that the temperatures measured along the tornado condensation funnel may have been representative of a *mixture* of both lofted dust and cloud droplets.

The further elevation of temperatures at the left and right edges of the warm tornado column (Fig. 9l) was probably the result of the centrifuging of relatively warm dust particles inside the funnel (Dowell *et al.* 2005) that is evident in the visible image (Fig. 9j). The edges of this cylinder of dust appeared darker than the rest of the funnel because more dust was present in a line-of-sight that passed from the camera location through either edge of the funnel. The warm edges of the warm tornado column are the infrared analog of the dark edges of the visible tornado dust sheath (Snow 1984). The sharp decrease in temperature at the right edge of the tornado just below the cloud base, which can be inferred from temperature trace LI01 (Fig. 9k, l), probably indicates that the relatively warm dust cloud did not reach the altitude of cloud base. Instead, the upper portion of the tornado contrasted against more distant clouds, which appeared colder as a result of the distance setting factor described in Section 2.

After the tornado crossed U.S. Highway 160, the condensation funnel became narrower as the tornado entered the dissipating "rope" stage of its life cycle. The upper half of the condensation funnel contrasted against more distant clouds (which appeared colder than the funnel), and the lower half of the funnel was obscured by a large, warm

dust cloud near the surface (Fig. 9m-o). The tornado dissipated at approximately 0108 UTC at a distance of 3.1 km to the northwest of the OU storm intercept team.

3) Deployment #3

At approximately 0114 UTC, another tornado touched down approximately 7 km west of the intersection of U.S. Highway 160 and Kansas State Highway 2 (Fig. 8). The storm intercept team was in the process of repositioning to a safe location as this tornado developed. One infrared image of the cloud base was captured during tornadogenesis (Fig. 9p-r). No visible RFD-generated clear slot was observed from the location of the infrared camera, and no temperature difference greater than that of instrument noise was observed across the base of the mesocyclone lowering (Fig. 9q, r). The dust-filled funnel moved slowly eastward over open fields for a distance of approximately 7 km and received a rating of F0 on the Fujita scale (NCDC 2004a).

A sequence of 13 infrared images was captured as the tornado approached the storm intercept team from the southwest, terminating when the team decided to reposition farther east along U.S. Highway 160 for safety. The final image in the sequence was captured from a distance of 2.5 km (Fig. 9s-u), and showed a very small increase in the temperature from left to right (on the order of 1 ºC) between the dust column of the tornado and its surroundings. Interestingly, the air to the left of the tornado funnel appeared cooler than the tornado funnel, while the air to the right of the tornado funnel appeared warmer than the tornado funnel. A small area of precipitation rotated from right to left around the back side of the tornado as the tornado developed, and then from left to right around the front side of the tornado as the tornado approached the storm intercept team, as evidenced by the 13 visible images associated with each of the 13 infrared

images in this sequence (not shown) and X-band radar reflectivity and Doppler velocity data collected during this deployment (not shown). This precipitation was located to the left and slightly in front of the tornado funnel at the time that the images in Fig. 9s-u were captured. At the same time, a visible dust cloud was seen extending to the right of the tornado (Fig. 9s), while any dust cloud on the left side of the tornado may have been suppressed by the approaching rain. In Fig. 9t, it appears that the encroaching precipitation curtain obscured the infrared signal from the left half of the tornado, while infrared signal from the right half remained relatively unobscured and was similar in appearance to that shown in Fig. 9k.

The tornado dissipated at approximately 0127 UTC, before the infrared camera could be deployed again.

b. 11 June 2004: Webster Co., Iowa

On 11 June 2004 (local time), a storm intercept team consisting of staff from the Center for Severe Weather Research (CSWR) and students from OU and Pennsylvania State University intercepted a tornado in central Iowa. Doppler radar data were collected in the tornado by two 3-cm wavelength Doppler on Wheels (DOW) radars (Wurman and Gill 2000).

The tornado appeared as a dust whirl in an open field approximately 2 miles (3.2 km) west of the town of Lehigh, Iowa at around 0026 UTC on 12 June 2004, and moved slowly eastward (Fig. 10). A visible clear slot generated by the RFD was readily apparent (Fig. 2). The storm intercept team, traveling eastward along Iowa State Highway 175, was initially located approximately 8 km south of the tornado. The DOW radar trucks

continued eastward along Iowa State Highway 175, while the vehicle containing the infrared camera equipment broke away from the team and headed north on Paragon Avenue for a distance of approximately 5.5 km. The infrared camera was deployed approximately 2 km south-southeast of the tornado (Fig. 3). A sequence of 10 infrared images was obtained between 0034 and 0038 UTC on 12 June 2004, capturing both the mature and shrinking stages of the tornado (Fig. 11).

Since the tornado had already been in progress for approximately 8 minutes before the infrared camera was deployed, no images were captured during the tornadogenesis phase. Because the deployment was delayed, the mesocyclone became occluded before any images could be captured, and any visual manifestation of the RFD had become unclear by the time of deployment. Unfortunately, a heavy rain curtain moved in between the infrared camera and the tornado (Fig. 12). This rain curtain completely obscured any infrared signal of the cloud base and tornado condensation funnel (Fig. 11b, e). As in Deployment #3 from 12 May 2004 in Harper County, a slight increase in temperature (on the order of 0.5 ºC or less) was measured from left to right along each of the temperature traces in Fig. 11b and e. This feature can be attributed to heavier precipitation on the left side of the image, which is apparent in the DOW reflectivity data collected during this deployment (Fig. 12).

The diameter of the tornado condensation funnel decreased, and then the tornado dissipated in this heavy rain at approximately 0039 UTC on 12 June. This tornado received a rating of F0, as it moved over open fields during its life cycle (NCDC 2004b).

4. SUMMARY AND CONCLUSIONS

During the spring seasons of 2003 and 2004, an infrared camera was deployed near supercell thunderstorms in an effort to capture infrared images of a mesocyclone cloud base during tornadogenesis. An atmospheric transmissivity study was conducted in order to ascertain an "ideal" range from which the infrared images of tornadoes should be captured; this range was calculated to be 1.5 – 3 km. Data from two case days were examined for which infrared images of tornadoes were captured. In the data collected on the first case day, very little appreciable temperature difference was observed along the mesocyclone cloud base prior to the formations of two separate tornadoes (Fig. 9e and Fig. 9p). (An earlier tornado condensation funnel [Fig. 9a-c] was too distant to be clearly detected by the infrared camera.) In the case of the second tornado, a slight temperature decrease (< 1 °C) was associated with the edges of the RFD clear slot, while the region on the interior of the RFD-generated clear slot appeared in the infrared imagery (Fig. 9e, h) as a slightly colder area. The relative contribution to this apparent temperature gradient that resulted from an actual temperature gradient along the cloud base, measurement error as described in Fig. 5c, or a combination of the two, is unclear. The two tornado condensation funnels imaged were found to be practically undetectable in the infrared images, while the dust clouds generated by the same tornadoes both appeared as vertical columns of slightly elevated temperatures. On the second case day, visual manifestations of the RFD were unclear by the time that the infrared camera could be deployed, and an intervening precipitation curtain completely obscured any infrared signal from the single tornado that was imaged and its associated cloud base.

In all but one of the images presented, the elevation angle of the infrared camera, when pointed at the underside of the mesocyclone, was too oblique to yield sufficiently

detailed information about temperature gradients along the mesocyclone cloud base. This result may indicate an inherent limitation of the method of study; obviously it would not be advisable to capture infrared images of a tornadic mesocyclone that is directly overhead! The only instance in which an infrared image of the underside of a tornadic mesocyclone was captured from almost directly underneath (Fig. 9p-r) occurred while the storm intercept team was hastily preparing to move away from an unsafe location. In this instance, no visible RFD was observed, and the image captured did not display any significant temperature gradient along the mesocyclone cloud base.

This study highlighted a number of additional difficulties inherent in infrared thermography in a severe thunderstorm situation. In particular:

- The temperature and humidity of the air at the location of the infrared camera can fluctuate greatly over short time periods and short distances in the immediate vicinity of a tornadic mesocyclone, potentially leading to erroneous temperature measurements. Ideally, a steady stream of independent temperature and relative humidity data would have to be collected at the location of the infrared camera, in order that each infrared image could be corrected to the best ability of the proprietary software. The distance from the infrared camera to the cloud base of interest must also be known accurately; the mobile Doppler radars described in this study furnished this information.
- The capture of infrared images of tornadogenesis is logistically challenging. Operators of the infrared camera in this study confronted many of the same challenges that those conducting previous *in situ* measurement studies in close

proximity to tornadic thunderstorms have encountered (e.g., poor road networks, hazardous deployment conditions, etc.). Often, a tornado is already in progress by the time the infrared camera can be deployed within the 1.5 to 3 km range.

- During Deployments #2 and #3 on 12 May 2004, any infrared signal from the tornado condensation funnel was found to be practically undetectable, i.e., it did not produce any change in measured temperature within the noise limits of the infrared camera (±2 ºC) unless the tornado contrasted against clouds that were significantly more distant (e.g. Fig. 9n). These observations may indicate that the air in the immediate environment surrounding the tornado was filled with lofted, infrared-emitting particles (dust), and therefore that any temperature gradient that existed between the tornado condensation funnel and its immediate, dust-filled environment was too weak to be detected using the infrared camera. It is important to note that both of these tornadoes occurred in the same storm and therefore in somewhat similar environments.
- As a consequence of the design of the infrared camera used, the temperature of the air in the cloud-free RFD could not be directly measured. The infrared camera was designed primarily for the examination of solid objects at close range, and as such, the infrared camera and its accompanying software are designed to *minimize* the effect of clear-air emissions on the measured temperatures. (The wavelength band used [8 – 12 m] is largely transparent to emissions from clear-air constituents.) The presence in the air of infrared emitting particles that were opaque in the 8 – 12 μm wavelength band (e.g. cloud droplets) was required in order to infer air temperatures. Temperature gradients were inferred from cloud

base temperature measurements at the interface between the RFD and the thunderstorm updraft, where entrainment and mixing were occurring, thinning the clouds and making the temperature measurements susceptible to the type of error depicted in Fig. 5c.

- The relatively high concentrations of haze and lofted soil particles in the warm sector decreased the infrared transmissivity of the atmosphere beyond what would be expected in the quiescent conditions of the atmospheric transmissivity study, requiring the infrared camera operator to decrease his or her range to the tornadic mesocyclone or tornado to less than the suggested range of 1.5 – 3 km.
- Precipitation curtains and/or lofted dust between the infrared camera and the tornado contaminated the infrared signal from the tornado funnel and cloud base; in some cases, the precipitation curtains and/or lofted dust completely obscured the tornado and/or cloud base.

At present, no single measurement system exists that can safely and practically provide thermodynamic data at sufficient spatial and temporal resolution necessary to measure the presence and extent of the RFD. In this study, we investigated the applicability of infrared thermal imaging to this endeavor, but found its applicability limited and the data sets difficult to collect with consistent quality. The sample size of cases highlighted in this paper is very small in comparison to the number that would be required in order to elucidate effectively a "typical" thermal structure of the mesocyclone cloud base. An "ideal" infrared camera deployment would require that images of tornadogenesis be captured from within the 1.5 – 3 km range, clearly showing the

presence of the temperature difference resulting from the presence of the RFD, and also including microscale *in situ* (unmanned aerial vehicle, e.g., Holland *et al.* 2001) measurements of the temperature and humidity at the ground (aloft). The infrared camera would need to be situated as close to the tornado as safely possible in order to obtain detailed temperature measurements across the underside of the mesocyclone cloud base. Additional experiments that could be performed include imaging the thunderstorm from an angle that would allow the RFD region to be viewed against the mesocyclone cloud base, where the type of errors described in Fig. 5c (which were encountered in one of the deployments) would be minimized.

This study proved to be an interesting exercise, and one well worth attempting if only to evaluate the suitability of the infrared camera technology to a meteorological application, and to ascertain its limitations. While the circumstances under which infrared thermography can be applied to measure temperature gradients in supercell updrafts are seriously constrained, horizontal and vertical temperature gradients in cloud bases and tornadoes (respectively) were successfully retrieved when those constraints were met. As demonstrated in the transmissivity study, infrared thermography can be used in conjunction with other *in situ* thermodynamic measuring systems in order to verify the measured temperatures and temperature gradients and maximize the usefulness of the technology in meteorological studies.

5. ACKNOWLEDGMENTS

Stephan P. Nelson of the National Science Foundation (NSF) supported this project under NSF SGER grant ATM-0332894 and NSF grant ATM-0241037. Gary Orlove of FLIR Systems, Inc. provided useful information about the transmissivity calculation algorithm in the proprietary ThermaCam software. Bradford S. Barrett and Daniel T. Dawson II of OU provided navigation for the first and third authors during field operations with the infrared camera. The authors are grateful to Dr. Joshua Wurman of the Center for Severe Weather Research in Boulder, Colorado, and Curtis R. Alexander of OU for allowing the infrared camera to join the DOW storm intercept team for a portion of each of the 2003 and 2004 storm seasons, and for sharing DOW radar data and operations logs for relevant cases. Dr. Ming Xue of the OU furnished the simulation results referred to in the section on the atmospheric transmissivity study. Dr. Joshua Wurman and two anonymous reviewers helped us to improve significantly the clarity of this manuscript.

6. REFERENCES

Berk, A., L. S. Bernstein, and D. C. Robertson, 1989: MODTRAN: A moderate-resolution model for LOWTRAN 7. GL-TR-89-0122. 38 pp. [NTIS AD A214337.]

Bluestein, H. B., 1983: Surface meteorological observations in severe thunderstorms. Part II: Field experiments with TOTO. *J. Appl. Meteor.,* **22**, 919 – 930.

———————, 1999: A history of severe-storm-intercept field programs. *Wea. Forecasting*, 14, 558 – 577.

———————, C. C. Weiss, and A. L. Pazmany, 2004: The vertical structure of a tornado near Happy, Texas, on 5 May 2002: High-resolution, mobile, W-band, Doppler radar observations. *Mon. Wea. Rev.,* **132**, 2325 – 2337.

———————, M. M. French, S. Frasier, K. Hardwick, F. Junyent, and A. Pazmany, 2005a: Dual-polarization observations of a tornado at close range made with a mobile, X-band Doppler radar. Preprints, *32nd Conf. on Radar Meteorology*, Albuquerque, NM, Amer. Meteor. Soc., CD-ROM, 10R.1.

———————, C. C. Weiss, E. Holthaus, S. Frasier, and A. Pazmany, 2005b: High-resolution, mobile, W-band, Doppler radar observations of the vertical structure of a tornado near Attica, Kansas on 12 May 2004. Preprints, *32nd Conf. on Radar Meteorology*, Albuquerque, NM, Amer. Meteor. Soc., CD-ROM, P15R.2.

Burnay, S. G., T. L. Williams, and C. H. Jones (Eds.), 1988: *Applications of Thermal Imaging*. Adam Hilger, 248 pp.

Craven, J. P., R. E. Jewell, and H. E. Brooks, 2002: Comparison between observed convective cloud-base heights and lifting condensation level for two different lifted parcels. *Wea. and Forecasting*, **17**, 885 – 890.

Curry, J. A., and P. J. Webster, 1999: *Thermodynamics of Atmospheres and Oceans*. Academic Press, 471 pp.

Davies-Jones, R. P., R. J. Trapp, and H. B. Bluestein, 2001: Tornadoes and tornadic storms. *Severe Convective Storms*, Meteor. Monogr., No. 28, Amer. Meteor. Soc., 167 – 221.

Doswell, C. A. III, 1985: The operational meteorology of convective weather. Vol. 2: Storm scale analysis. NOAA Tech. Memo. ERL ESG-15, 240 pp.

Dowell, D. C., and H. B. Bluestein, 1997: The Arcadia, Oklahoma storm of 17 May 1981: Analysis of a supercell during tornadogenesis. *Mon. Wea. Rev.*, **125**, 2562 – 2582.

————————, and ————————, 2002: The 8 June 1995 McLean, Texas, storm: Part I: Observations of cyclic tornadogenesis. *Mon. Wea. Rev.*, **130**, 2626 – 2648.

————————, C. A. Alexander, J. Wurman, and L. J. Wicker, 2005: Centrifuging of hydrometeors and debris in tornadoes: Radar-reflectivity patterns and wind-measurement errors. *Mon. Wea. Rev.*, **133**, 1501 – 1524.

Hayes, C., 2004: Tornado outbreak in Harper County, Kansas on 05/12/04. [Report from the National Weather Service – Wichita, Kansas office, available online at http://www.crh.noaa.gov/ict/cgi-bin/vuestory.pl?STORY_NUMBER=2004051418.]

Holland, G. J., P. J. Webster, J. A. Curry, G. Tyrell, D. Gauntlett, G. Brett, J. Becker, R. Hoag, and W. Vaglienti, 2001: The Aerosonde robotic aircraft: A new paradigm for environmental observations. *Bull. Amer. Meteor. Soc.*, **82**, 889 – 901.

Holst, G. C., 2000: *Common Sense Approach to Thermal Imaging*. SPIE Optical Engineering Press, 377 pp.

Kidder, S. Q., and T. H. Vonder Haar, 1995: *Satellite Meteorology: An Introduction*. Academic Press, 466 pp.

Knuteson, R. O., H. E. Revercomb, F. A. Best, N. C. Ciganovich, R. G. Dedecker, T. P. Dirkx, S. C. Ellington, W. F. Feltz, R. K. Garcia, H. B. Howell, W. L. Smith, J. F. Short and D. C. Tobin, 2004: Atmospheric Emitted Radiance Interferometer. Part I: Instrument design. *J. Atmos. Oceanic Technol.*, **21**, 1763 – 1776.

Kramar, M. R., H. B. Bluestein, A. L. Pazmany, and J. D. Tuttle, 2005: The "Owl Horn" radar signature in developing Southern Plains supercells. *Mon. Wea. Rev.*, **133**, 2608 – 2634.

Lemon, L. R., and C. A. Doswell III, 1979: Severe thunderstorm evolution and mesocyclone structure as related to tornadogenesis. *Mon. Wea. Rev.*, **107**, 1184 – 1197.

Liou, K. N., 2002: *An Introduction to Atmospheric Radiation.* 2nd ed. Academic Press, 583 pp.

Markowski, P. M. 2002a: Hook echoes and rear-flank downdrafts: A review. *Mon. Wea. Rev.*: **130**, 852 – 876.

————————, 2002b: Mobile mesonet observations on 3 May 1999. *Wea. and Forecasting*, **17**, 430 – 444.

————————, J. M. Straka, and E. N. Rasmussen, 2002: Direct surface observations within the rear-flank downdrafts of non-tornadic and tornadic supercells. *Mon. Wea. Rev.*, **130**, 1692 – 1721.

NCDC, 2004a. *Storm Data*. Vol. 46, No. 5, 586 pp. [Available online at http://www5.ncdc.noaa.gov/pubs/publications.html.]

————————, 2004b. *Storm Data*. Vol. 46, No. 6, 450 pp. [Available online at http://www5.ncdc.noaa.gov/pubs/publications.html.]

Rotunno, R., and J. Klemp, 1985: On the rotation and propagation of simulated supercell thunderstorms. *J. Atmos. Sci.*, 42, 271 – 292.

Snow, J., 1984: On the formation of particle sheaths in columnar vortices. *J. Atmos. Sci.*, **41**, 2477 – 2491.

Wallace, J. M, and P. V. Hobbs, 1977: *Atmospheric Science: An Introductory Survey.* Academic Press, 467 pp.

Wurman, J. and S. Gill, 2000: Finescale radar observations of the Dimmitt, Texas (2 June 1995), tornado. *Mon. Wea. Rev.,* **128**, 2135 – 2164.

7. LIST OF FIGURES

Fig. 1. Conceptual model of the surface-level wind fields in and around a supercell thunderstorm in the northern hemisphere. The locations of the forward-flank downdraft (FFD) and rear-flank downdraft (RFD) are represented by the two regions shaded dark gray. The primary thunderstorm updraft (UD) and smaller updrafts along the gust front are denoted by the regions shaded light gray. The forward-flank gust front (FFGF) and rear-flank gust front (RFGF) wind shifts are denoted by dotted lines. The southern "T" represents a favorable location for tornado development, and to the west of the northern "T" a favorable location for tornado decay (e. g., Dowell and Bluestein 2002). Adapted from Lemon and Doswell (1979) and Davies-Jones (1986).

Fig. 2. Still frame from a video of a tornado near Lehigh, Iowa, on 11 June 2004, showing the "clear slot" associated with the RFD (light area above and to the left of the tornado at cloud base). The appearance of the clear slot preceded the appearance of the tornado by approximately two minutes. Video © R. Tanamachi.

Fig. 3. Still frame from a video showing the first author using the infrared camera to capture images of a tornado near Lehigh, Iowa on 11 June 2004 (local time). Video © R. Tanamachi.

Fig. 4. The FLIR brand S60 infrared thermal imaging camera used in this study. Image © FLIR Systems, Inc.

Fig. 5. Explanations of erroneous cloud temperature readings by the infrared camera during the atmospheric transmissivity study. (a) Changes with elevation angle: A cloud viewed via line-of-sight A will appear warmer than a cloud viewed via line-of-sight B. (b) Changes with camera distance setting. (c) Changes with cloud opacity/optical

thickness. In our atmospheric transmissivity study, the effect described in (a) dominated the effects described in (b) and (c).

Fig. 6. (a) Visible and (b) infrared thermal images captured on 18 May 2004 as part of the transmissivity study, showing the reduced optical depth close to the horizon owing to relatively high concentrations of IR-emitting gases and particles in the planetary boundary layer.

Fig. 7. Difference in LCL temperature calculated from NWS rawinsonde measurements of the lowest 500 m of the atmosphere and cloud-base temperature measured by the infrared camera at 00 UTC on 15, 19, and 21 May 2004. Horizontal error bars account for the uncertainty in rawinsonde-calculated LCL altitude (Craven et al. 2002). Surface temperature and relative humidity are indicated in the legend. Measurements of the clear sky were also taken on 14 and 20 May as a control. The shaded box encloses a span of optimum camera-to-cloud distance (1.5 to 3.0 km). The two indicated data points that fall outside the primary cluster of data points inside the shaded region are both instances of optically thin clouds. The distance scale (in m) is logarithmic.

Fig. 8. Map of infrared camera deployment locations (black dots, with viewing directions indicated) and tornado paths (thick gray lines labeled with Fujita scale ratings) in Harper Co., Kansas on 12 May 2004 (local time). Adapted from Hayes (2004), base map from Google Maps © 2005.

Fig. 9. (a) Visible (contrast enhanced for visibility) and (b) infrared thermal images of a tornado near Sharon, Kansas on 12 May 2004 at 2320 UTC. (c) Measured temperatures along the labeled lines in the infrared thermal image. The view was to the southeast. The tornado was approximately 5.0 km from the infrared camera and was moving very

slowly. (d) Visible and (e) infrared thermal images of a developing tornado near Attica, Kansas on 12 May 2004 at 2355 UTC. (f) Measured temperatures along the labeled lines in the infrared thermal image. The view was to the west-southwest. The upward "bowing" of the isotherms near the left and right edges of the image is a result of the warming of the edges of the infrared sensor array inside the infrared camera; the infrared sensors are internally re-calibrated approximately every 15 seconds. (g) – (i) as in (d) – (f) but at 2356 UTC on 12 May 2004. The view was to the west-southwest. The tornado was approximately 2.8 km from the infrared camera. (j) – (l) as in (d) – (f) but at 0002 UTC on 13 May 2004. The view was to the west. The tornado was approximately 3.0 km from the camera and was moving from left to right across the image. The bright, cold area at the upper right of the tornado condensation funnel represents clouds that were located at a significantly larger distance from the infrared camera than the tornado and its associated cloud base (dark gray clouds at upper right). (m) – (o) as in (d) – (f) but at 0004 UTC on 13 May 2004. The view was to the west-northwest. The tornado was approximately 3.1 km from the infrared camera. The bright, cold area behind the upper portion of the tornado condensation funnel represents clouds that were located at a significantly larger distance from the infrared camera than the tornado and its associated cloud base (dark gray clouds at upper right). (p) Visible and (q) infrared thermal images of a rotating cloud lowering that later formed a tornado near Harper, Kansas on 13 May 2004 at 0014 UTC. (d) Measured temperatures along the labeled lines in the infrared thermal image. The cloud lowering was located above and slightly to the south of the thermographer. (s) Visible and (t) infrared thermal images of a tornado near Harper, Kansas on 13 May 2004 at 0024 UTC. (u) Measured temperatures along the labeled lines

in the infrared thermal image. The view was to the southwest. The exact distance from the camera to the tornado is unknown, but was estimated to have been approximately 2.4 km.

Fig. 10. Map of infrared camera deployment location (black dot with viewing direction indicated) and tornado path (thick gray line labeled with Fujita scale rating) in Webster Co., Iowa on 11 June 2004 (local time). Base map from Google Maps © 2005.

Fig. 11. (a) Visible and (b) infrared thermal images of a tornado near Lehigh, Iowa on 12 June 2004 at 0035 UTC. (c) Measured temperatures along the labeled lines in the infrared thermal image. The view was to the north-northwest. The tornado was approximately 2.7 km from the infrared camera and was moving very slowly from left to right. (continued)

Fig. 12. DOW Doppler velocity (top) and reflectivity data (bottom) collected at 0035 UTC on 12 June 2004 near Lehigh, Iowa, in the tornado pictured in Fig. 14. The range rings are in km, the velocity scale is in m s^{-1}, and the reflectivity scale is in dBZ. The location of the tornado is indicated in the Doppler velocity image by the velocity couplet, and in the reflectivity image by the weak-echo hole. The location and the viewing angle of the infrared camera are indicated by the white dot.

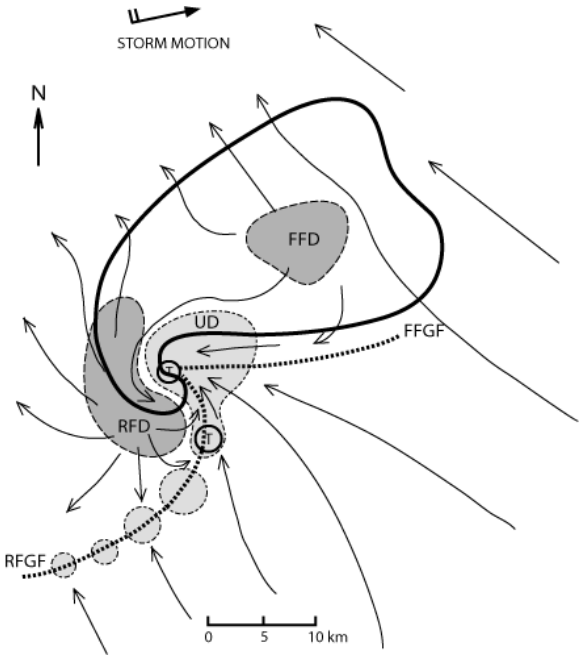

Fig. 1. Conceptual model of the surface-level wind fields in and around a supercell thunderstorm in the northern hemisphere. The locations of the forward-flank downdraft (FFD) and rear-flank downdraft (RFD) are represented by the two regions shaded dark gray. The primary thunderstorm updraft (UD) and smaller updrafts along the gust front are denoted by the regions shaded light gray. The forward-flank gust front (FFGF) and rear-flank gust front (RFGF) wind shifts are denoted by dotted lines. The southern "T" represents a favorable location for tornado development, and to the west of the northern "T" a favorable location for tornado decay (e. g., Dowell and Bluestein 2002). Adapted from Lemon and Doswell (1979) and Davies-Jones (1986).

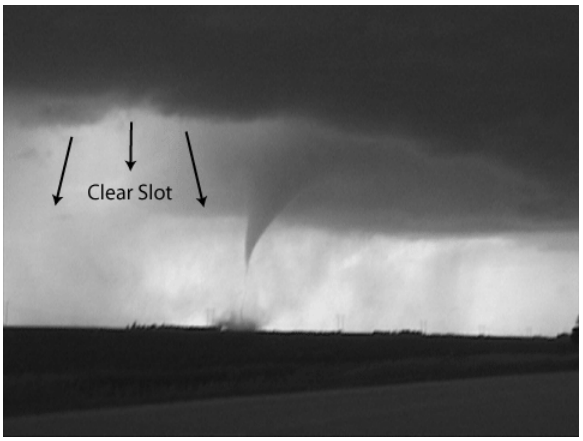

Fig. 2. Still frame from a video of a tornado near Lehigh, Iowa, on 11 June 2004, showing the "clear slot" associated with the RFD (light area above and to the left of the tornado at cloud base). The appearance of the clear slot preceded the appearance of the tornado by approximately two minutes. Video © R. Tanamachi.

Fig. 3. Still frame from a video showing the first author using the infrared camera to capture images of a tornado near Lehigh, Iowa on 11 June 2004 (local time). Video © R. Tanamachi.

Fig. 4. The FLIR brand S60 infrared thermal imaging camera used in this study. Image © FLIR Systems, Inc.

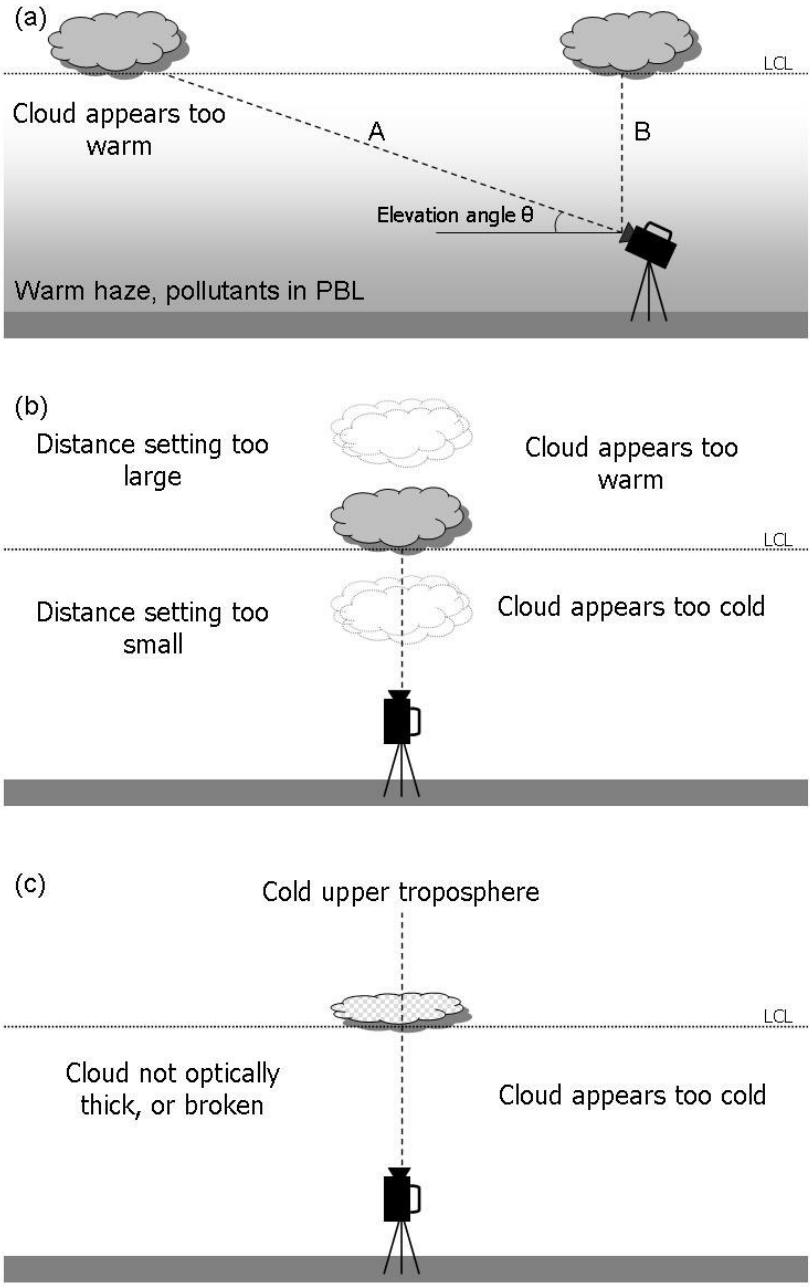

Fig. 5. Explanations of erroneous cloud temperature readings by the infrared camera during the atmospheric transmissivity study. (a) Changes with elevation angle: A cloud viewed via line-of-sight A will appear warmer than a cloud viewed via line-of-sight B. (b) Changes with camera distance setting. (c) Changes with cloud opacity/optical thickness. In our atmospheric transmissivity study, the effect described in (a) dominated the effects described in (b) and (c).

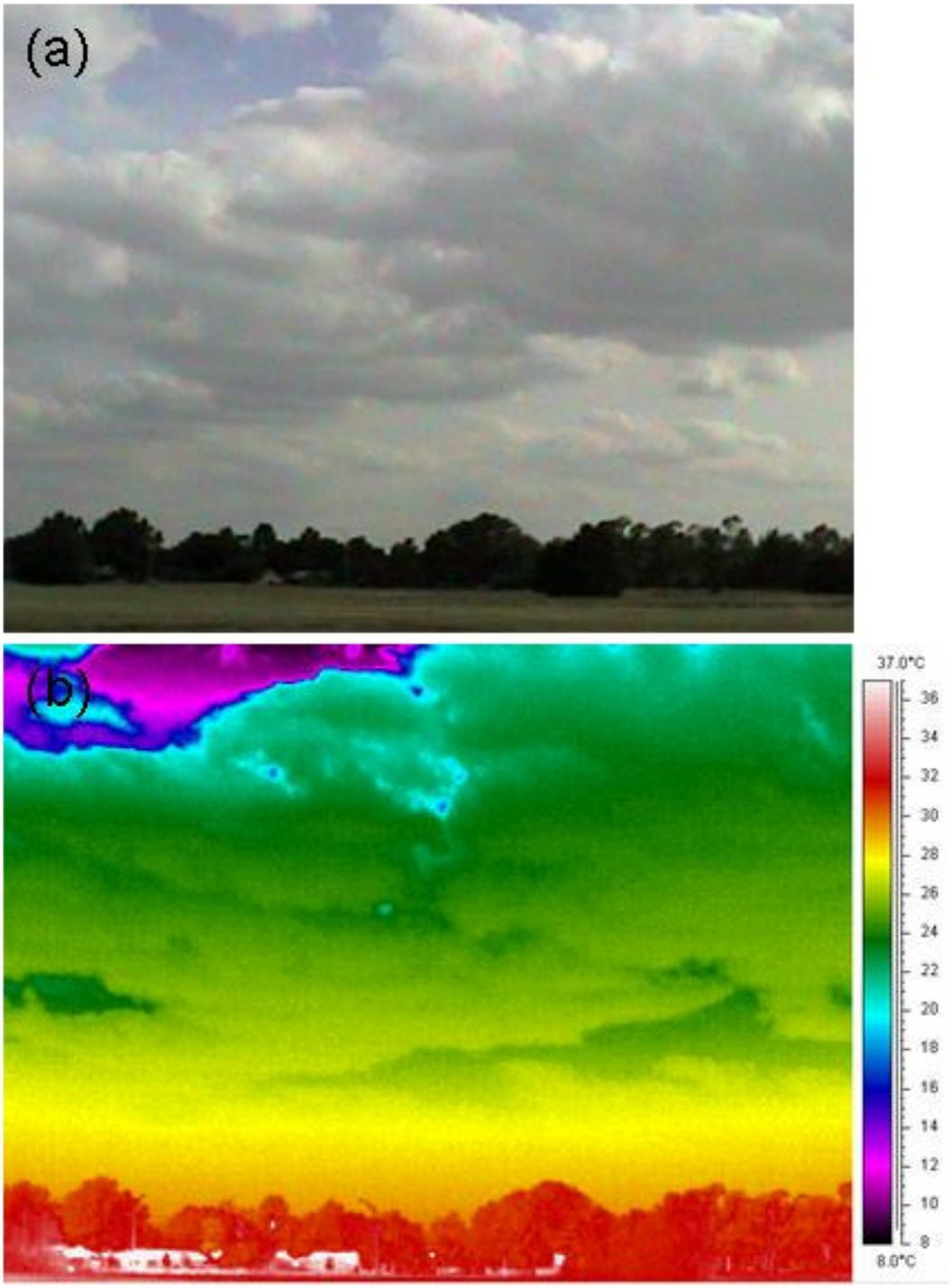

Fig. 6. (a) Visible and (b) infrared thermal images captured on 18 May 2004 as part of the transmissivity study, showing the reduced optical depth close to the horizon owing to relatively high concentrations of IR-emitting gases and particles in the planetary boundary layer.

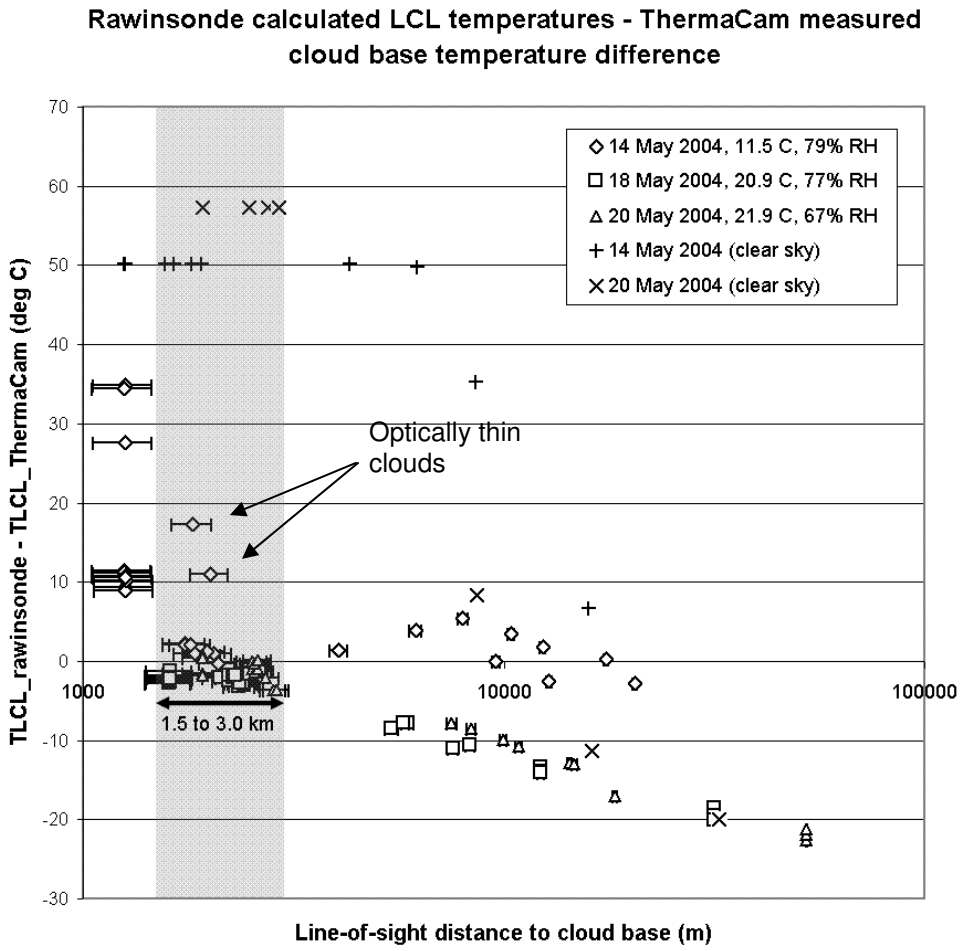

Fig. 7. Difference in LCL temperature calculated from NWS rawinsonde measurements of the lowest 500 m of the atmosphere and cloud-base temperature measured by the infrared camera at 00 UTC on 15, 19, and 21 May 2004. Horizontal error bars account for the uncertainty in rawinsonde-calculated LCL altitude (Craven et al. 2002). Surface temperature and relative humidity are indicated in the legend. Measurements of the clear sky were also taken on 14 and 20 May as a control. The shaded box encloses a span of optimum camera-to-cloud distance (1.5 to 3.0 km). The two indicated data points that fall outside the primary cluster of data points inside the shaded region are both instances of optically thin clouds. The distance scale (in m) is logarithmic.

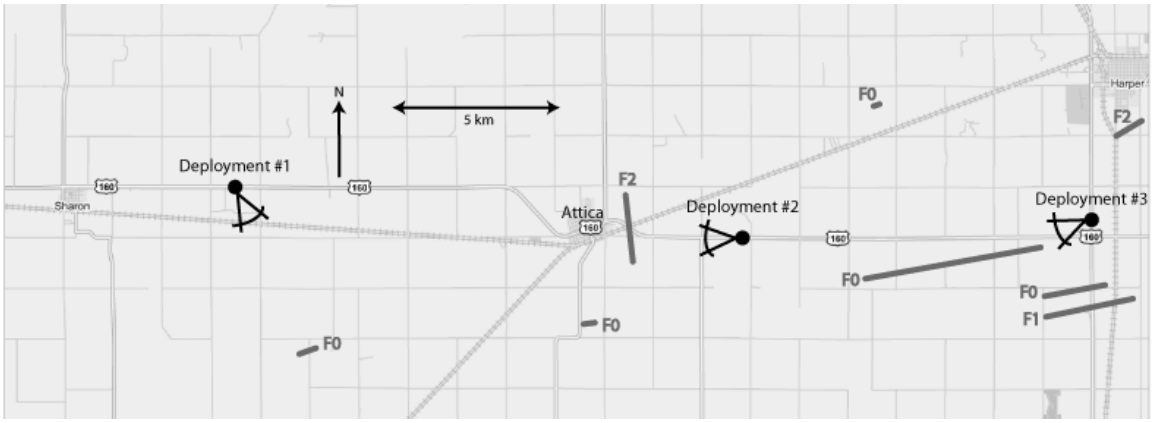

Fig. 8. Map of infrared camera deployment locations (black dots, with viewing directions indicated) and tornado paths (thick gray lines labeled with Fujita scale ratings) in Harper Co., Kansas on 12 May 2004 (local time). Adapted from Hayes (2004), base map from Google Maps © 2005.

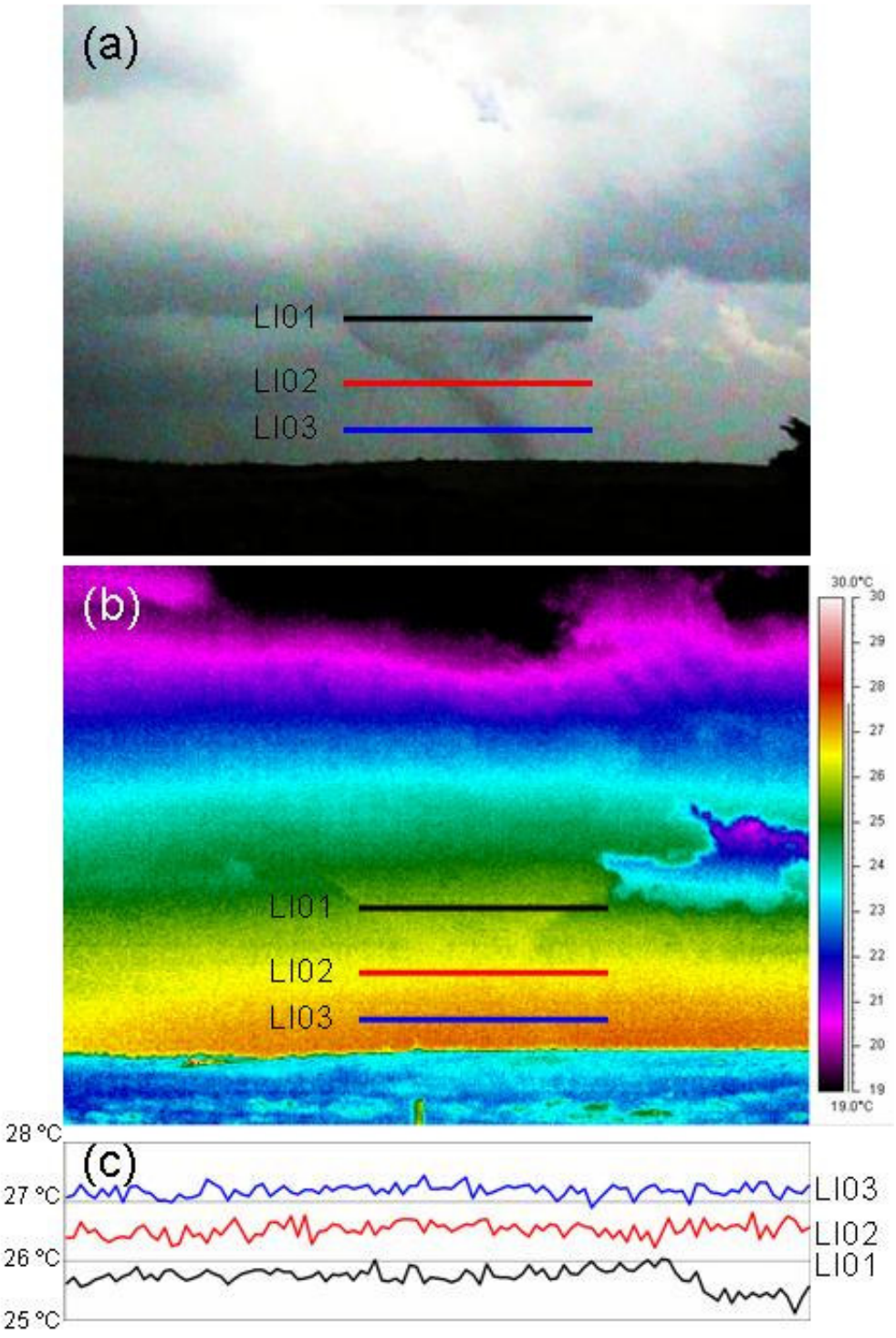

Fig. 9. (a) Visible (contrast enhanced for visibility) and (b) infrared thermal images of a tornado near Sharon, Kansas on 12 May 2004 at 0020 UTC. (c) Measured temperatures along the labeled lines in the infrared thermal image. The view was to the southeast. The tornado was approximately 5.0 km from the infrared camera and was moving very slowly. (continued)

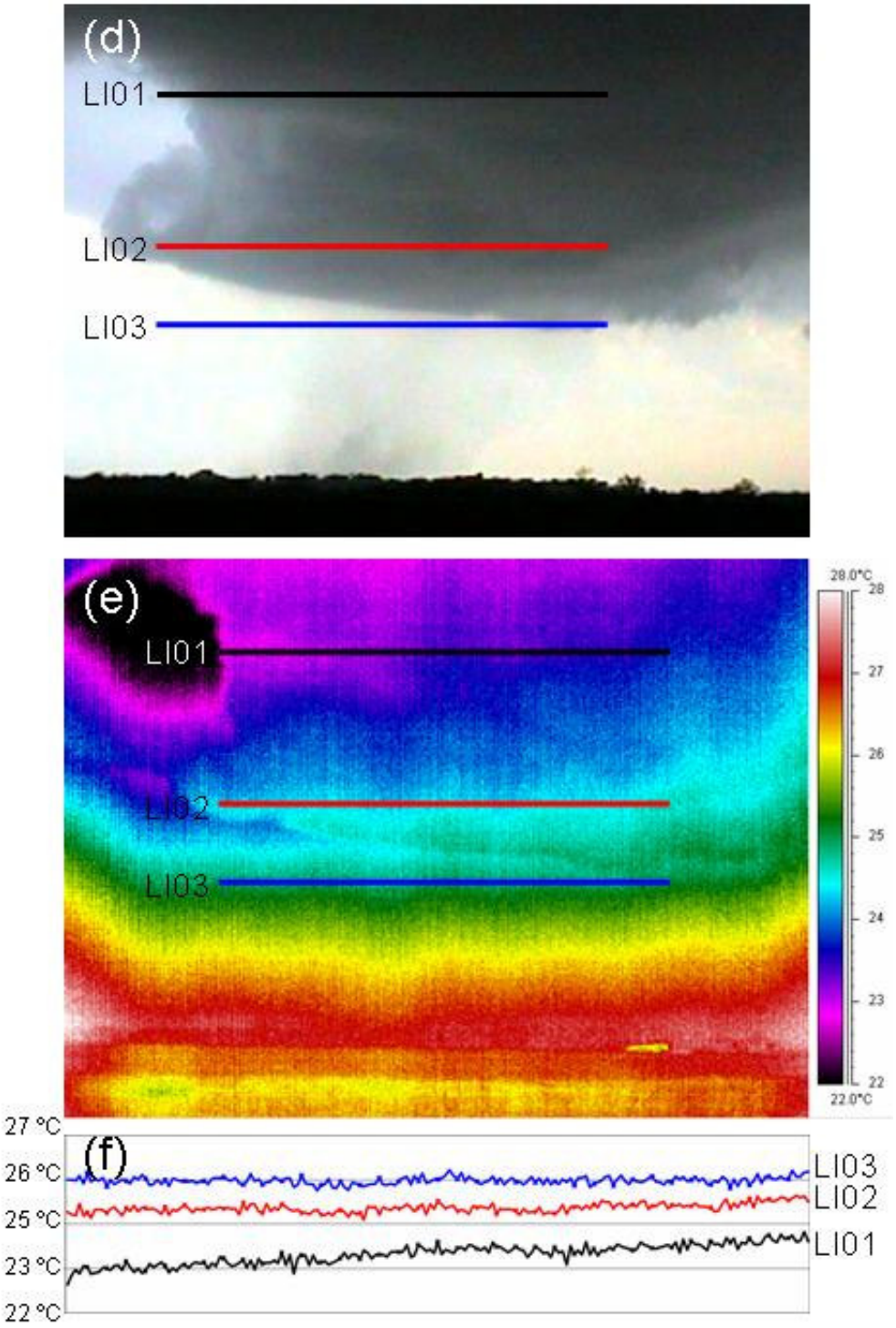

Fig. 9 (continued). (d) Visible and (e) infrared thermal images of a developing tornado near Attica, Kansas on 12 May 2004 at 0055 UTC. (f) Measured temperatures along the labeled lines in the infrared thermal image. The view was to the west-southwest. The upward "bowing" of the isotherms near the left and right edges of the image is a result of the warming of the edges of the infrared sensor array inside the infrared camera; the infrared sensors are internally re-calibrated approximately every 15 seconds. (continued)

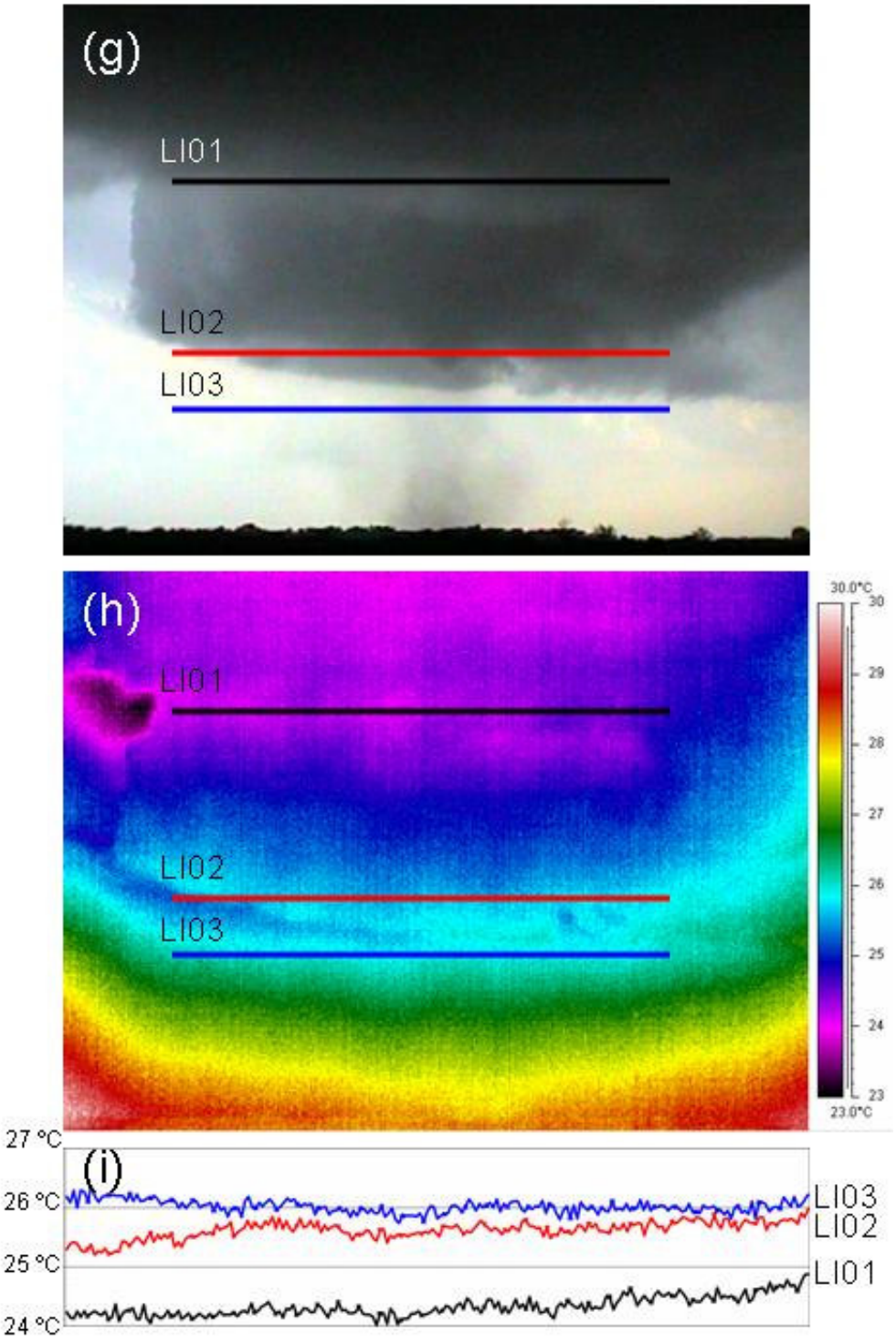

Fig. 9 (continued). (g) – (i) as in (d) – (f) but at 0056 UTC on 12 May 2004. The view was to the west-southwest. The tornado was approximately 2.8 km from the infrared camera. (continued)

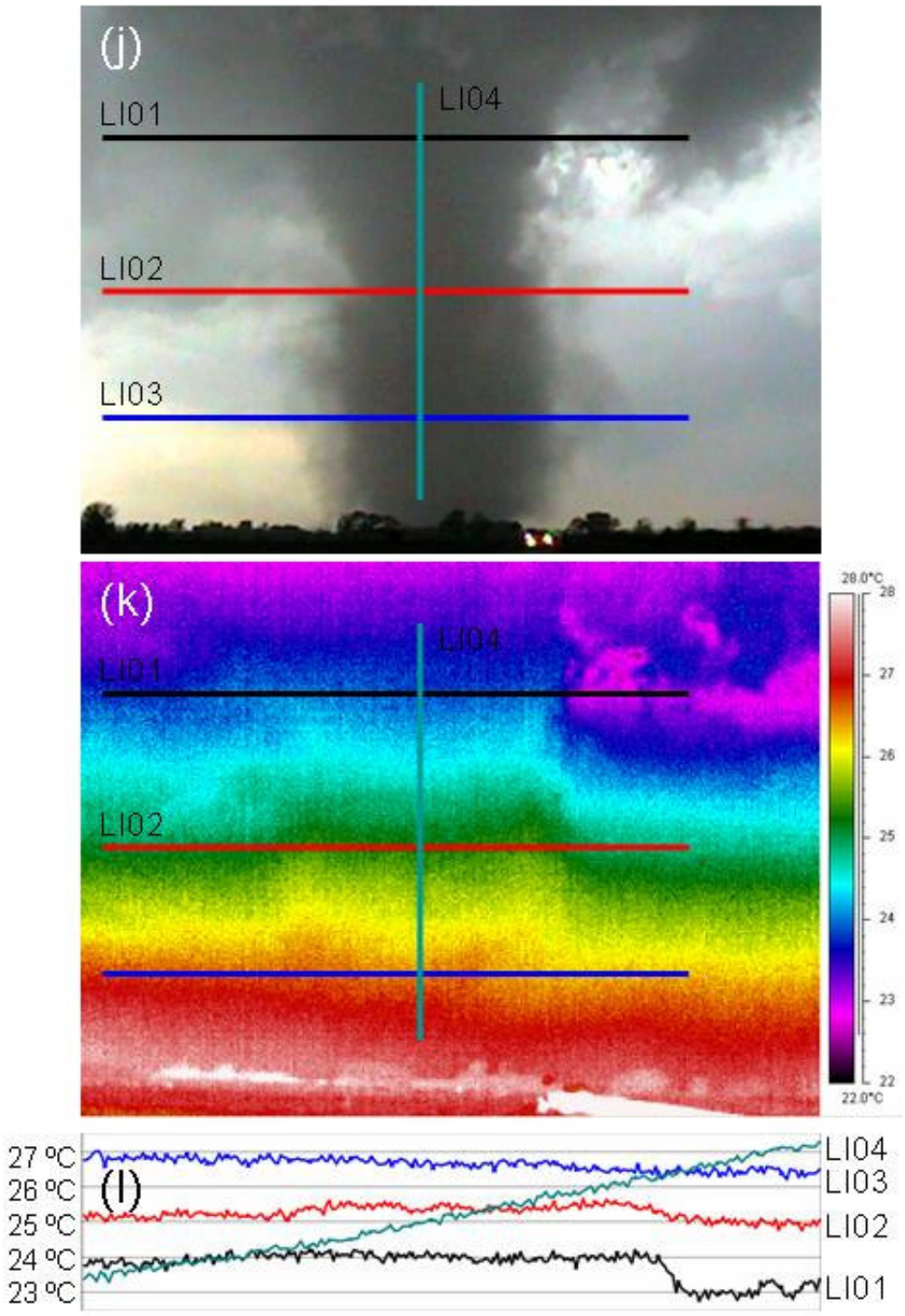

Fig. 9 (continued). (j) – (l) as in (d) – (f) but at 0102 UTC on 13 May 2004. The view was to the west. The tornado was approximately 3.0 km from the camera and was moving from left to right across the image. The bright, cold area at the upper right of the tornado condensation funnel represents clouds that were located at a significantly longer distance from the infrared camera than the tornado and its associated cloud base (dark gray clouds at upper right). (continued)

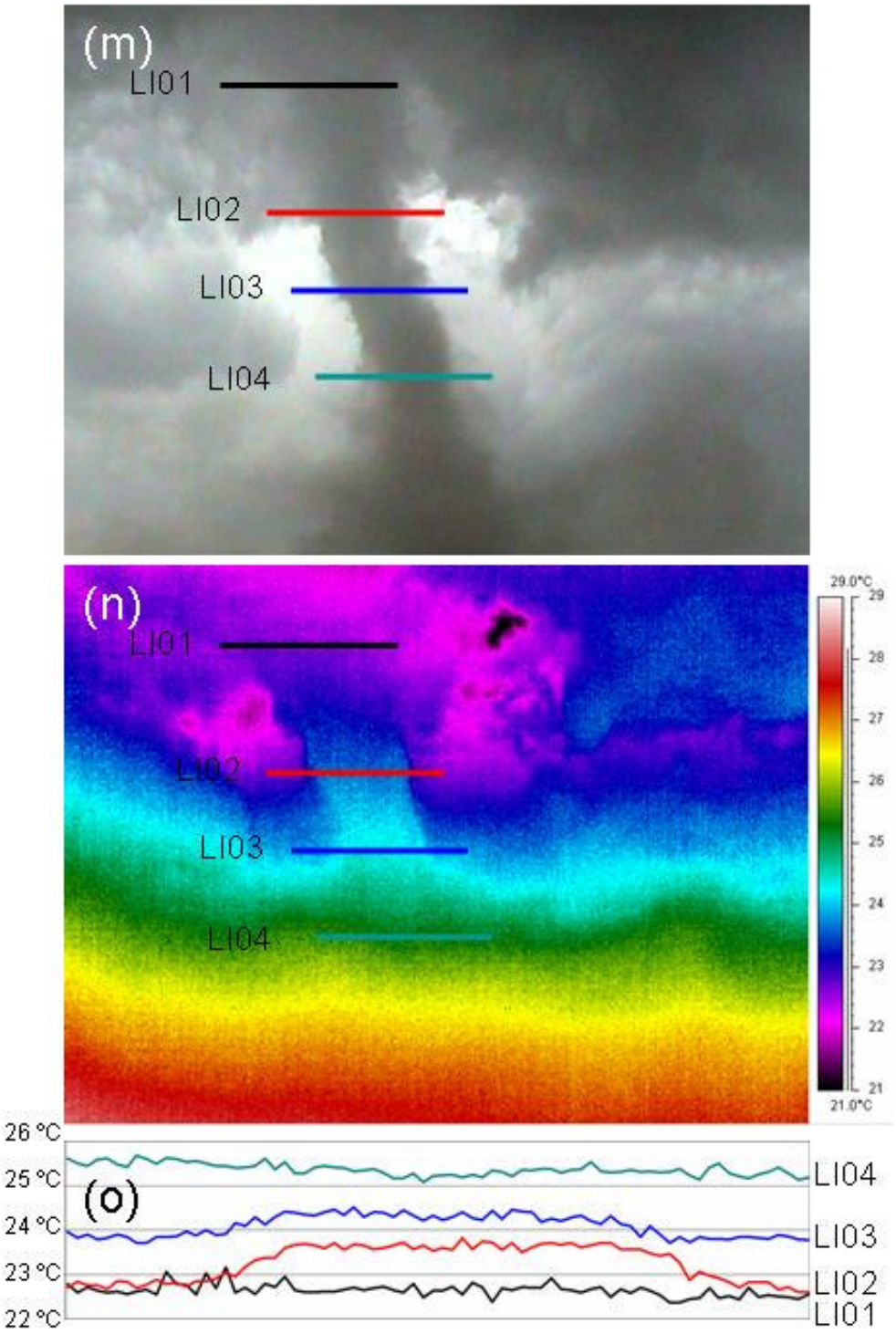

Fig. 9 (continued). (m) – (o) as in (d) – (f) but at 0104 UTC on 13 May 2004. The view was to the west-northwest. The tornado was approximately 3.1 km from the infrared camera. The bright, cold area behind the upper portion of the tornado condensation funnel represents clouds that were located at a significantly longer distance from the infrared camera than the tornado and its associated cloud base (dark gray clouds at upper right). (continued)

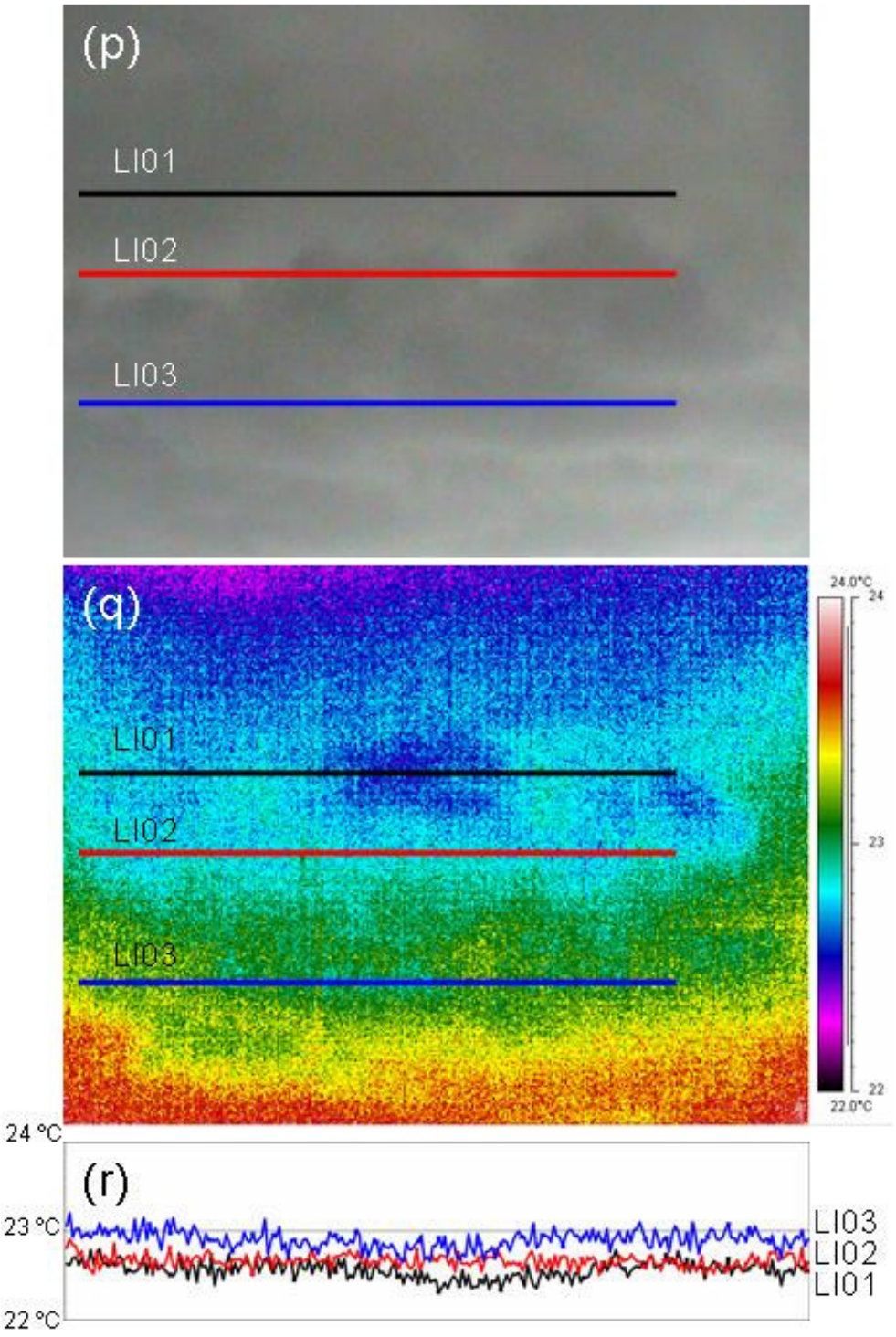

Fig. 9 (continued). (p) Visible and (q) infrared thermal images of a rotating cloud lowering that later formed a tornado near Harper, Kansas on 13 May 2004 at 0114 UTC. (d) Measured temperatures along the labeled lines in the infrared thermal image. The cloud lowering was located above and slightly to the south of the thermographer. (continued)

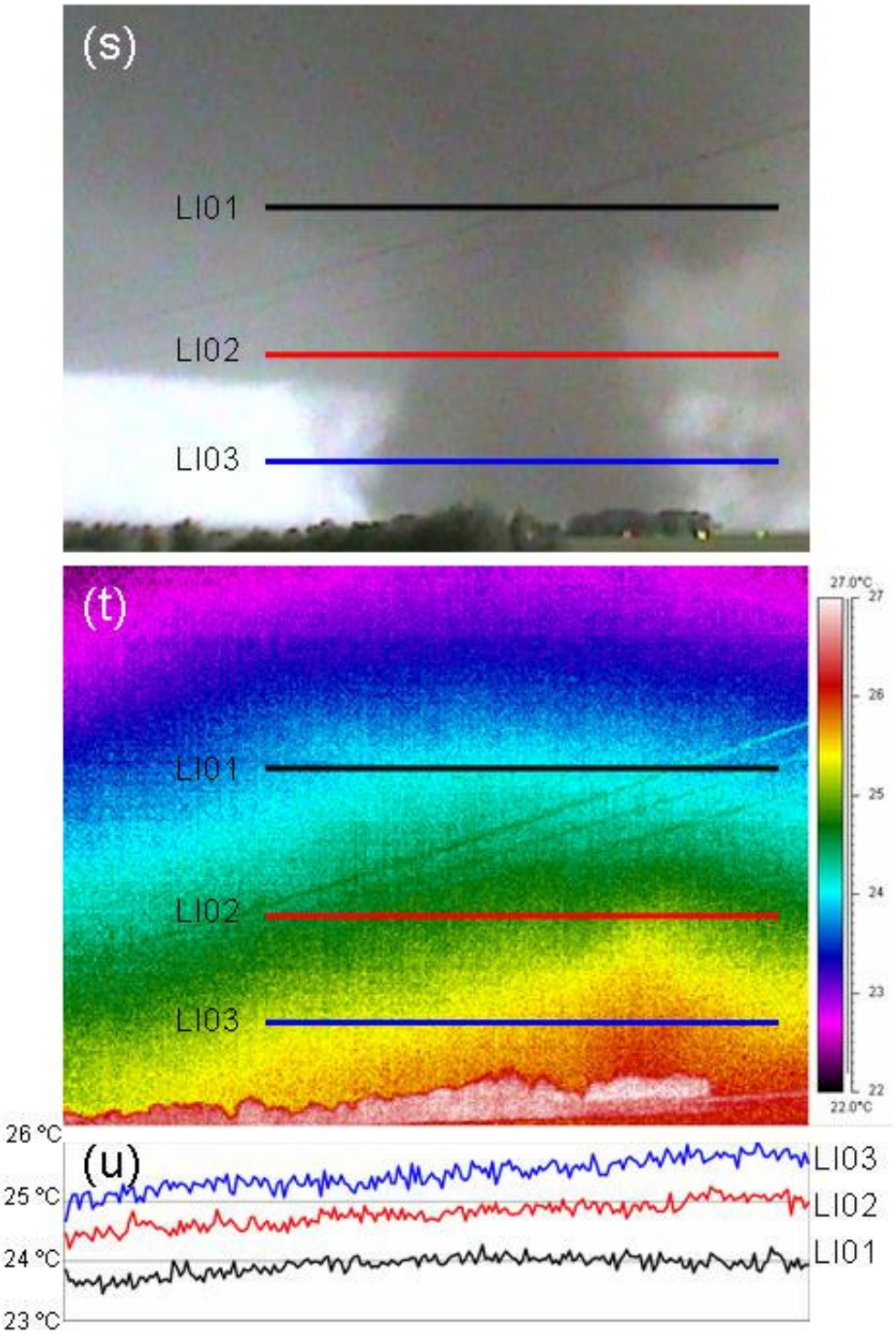

Fig. 9 (continued). (s) Visible and (t) infrared thermal images of a tornado near Harper, Kansas on 13 May 2004 at 0124 UTC. (u) Measured temperatures along the labeled lines in the infrared thermal image. The view was to the southwest. The exact distance from the camera to the tornado is unknown, but was estimated to have been approximately 2.4 km.

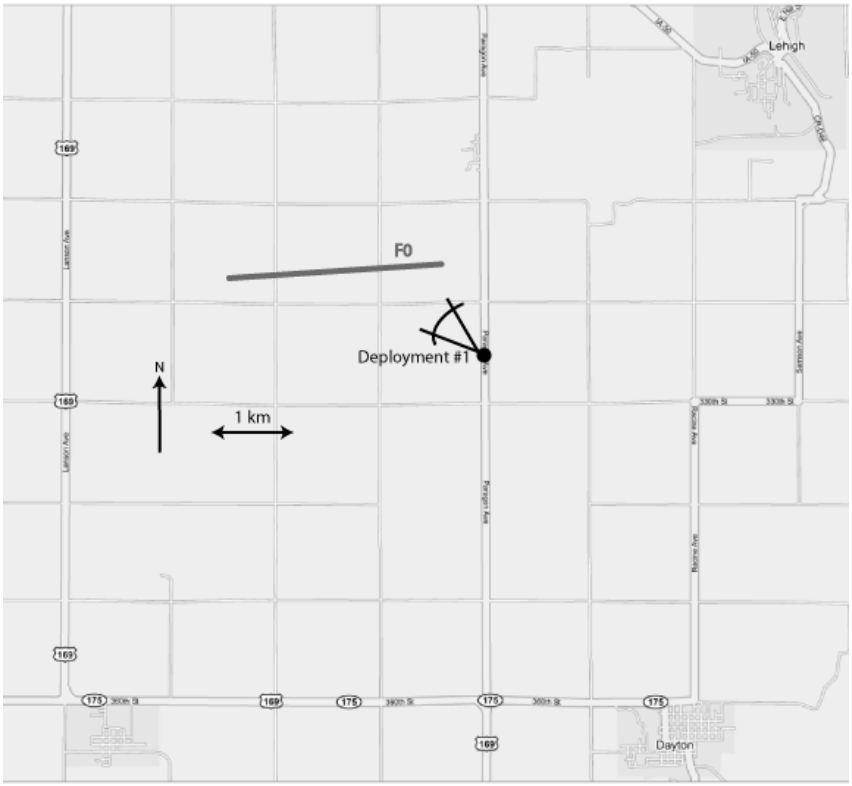

Fig. 10. Map of infrared camera deployment location (black dot with viewing direction indicated) and tornado path (thick gray line labeled with Fujita scale rating) in Webster Co., Iowa on 11 June 2004 (local time). Base map from Google Maps © 2005.

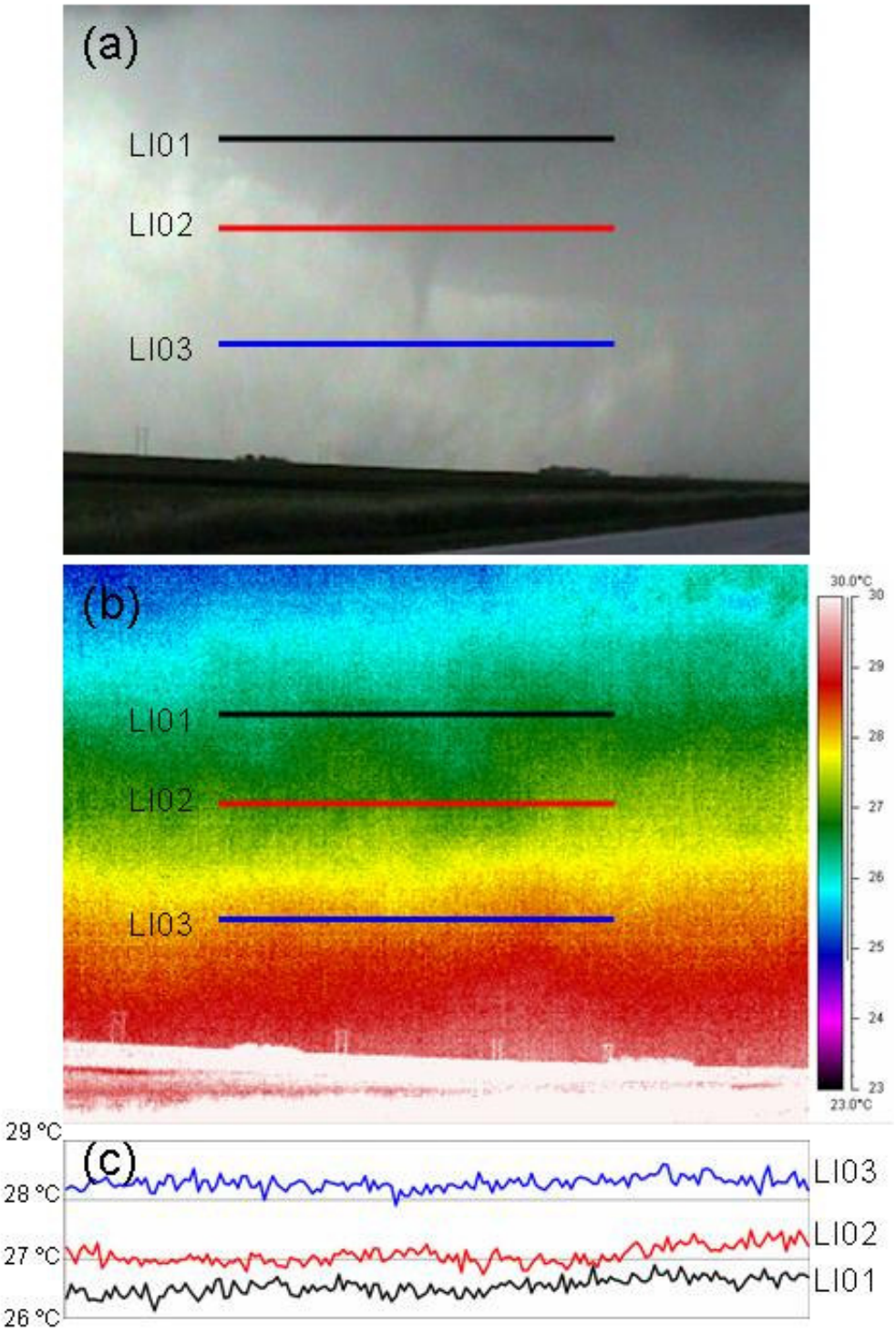

Fig. 11. (a) Visible and (b) infrared thermal images of a tornado near Lehigh, Iowa on 12 June 2004 at 0035 UTC. (c) Measured temperatures along the labeled lines in the infrared thermal image. The view was to the north-northwest. The tornado was approximately 2.7 km from the infrared camera and was moving very slowly from left to right. (continued)

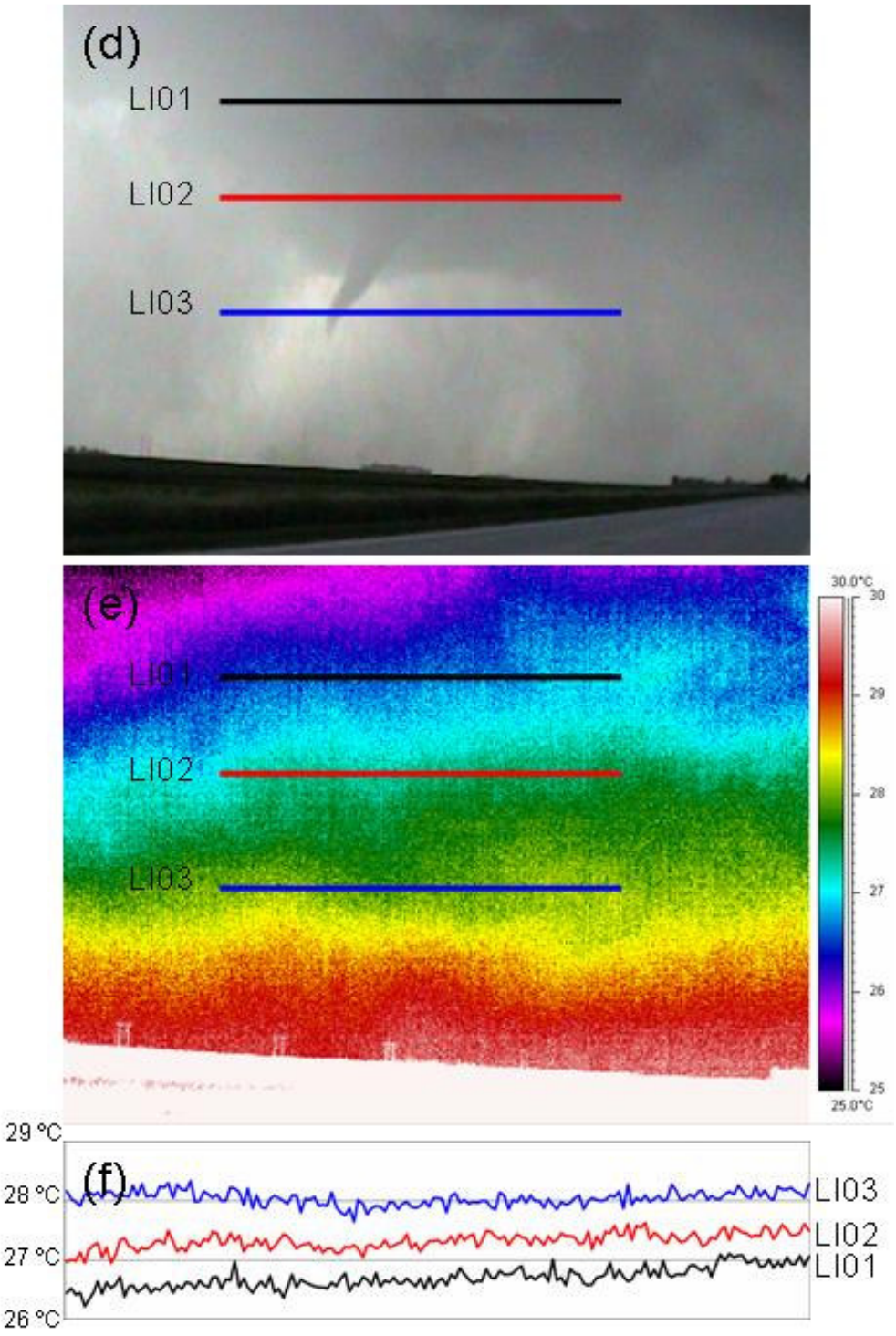

Fig. 11 (continued). (d) – (f) as in (a) – (c) but at 0036 UTC on 12 June 2004. The precipitation on the left side of the image was much closer to the infrared camera than that at the right. The former is indicative of an advancing gust front, which was moving from left to right across the image.

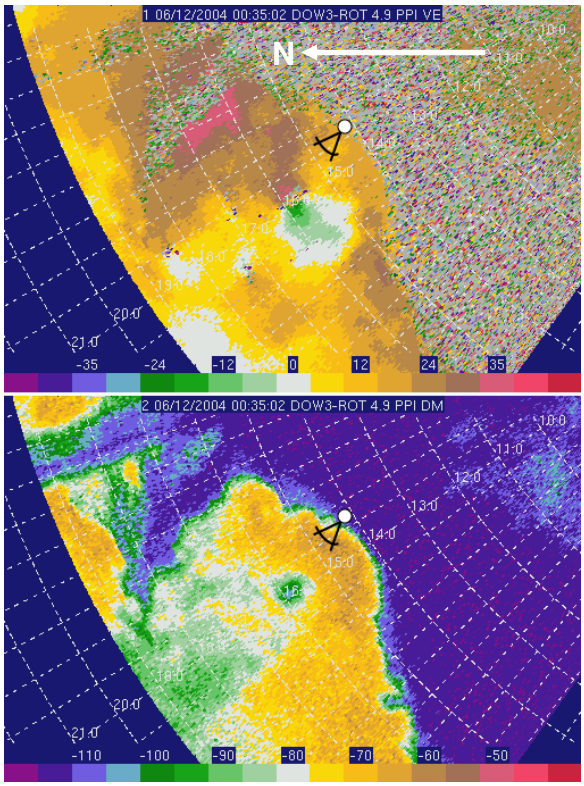

Fig. 12. DOW Doppler velocity (top) and reflectivity data (bottom) collected at 0035 UTC on 12 June 2004 near Lehigh, Iowa, in the tornado pictured in Fig. 11. The range rings are in km, the velocity scale is in m s^{-1}, and the reflectivity scale is in dBZ. The location of the tornado is indicated in the Doppler velocity image by the velocity couplet, and in the reflectivity image by the weak-echo hole. The location and the viewing angle of the infrared camera are indicated by the white dot.